

Development of fcc-Al nanoparticles during crystallization of amorphous Al–Ni alloys containing mischmetal: Microstructure and hardness evaluation

M. Mansouri^a, A. Simchi^{a,b,*}, N. Varahram^a, E.S. Park^c

^a Department of Materials Science and Engineering, Sharif University of Technology, 14588 Tehran, Iran

^b Institute for Nanoscience and Nanotechnology, Sharif University of Technology, 14588 Tehran, Iran

^c Research Institute of Advanced Materials, Department of Materials Science and Engineering, Seoul National University, Seoul 151-744, Republic of Korea

ARTICLE INFO

Article history:

Received 17 December 2013

Received in revised form

26 February 2014

Accepted 2 March 2014

Available online 12 March 2014

Keywords:

Aluminum alloy
Rapid solidification
Crystallization
Microstructure
Nanoindentation

ABSTRACT

In the present work, fcc-Al nanoparticle development in $\text{Al}_{90-x}\text{Ni}_{10}\text{MM}_x$ (MM: Ce mischmetal; $x=2, 4$) amorphous alloys was studied via non-isothermal differential scanning calorimetry, X-ray diffraction, transmission electron microscopy, and nanoindentation test. Results showed that the crystallization of $\text{Al}_{88}\text{Ni}_{10}\text{MM}_2$ alloy occurred by the precipitation of fcc-Al nanoparticles followed by the crystallization of $\text{Al}_{11}\text{MM}_3$ and Al_3Ni phases. Transmission electron microscopy revealed that the aluminum precipitates had an average size of ~ 12 nm with a round morphology. Increasing the mischmetal content to 4 at% ($\text{Al}_{86}\text{Ni}_{10}\text{MM}_4$ alloy) caused a three-stage crystallization process with a change in the size and morphology of fcc-Al precipitates. Here, fcc-Al nanoparticles got an irregular and cluster-like morphology with an average size of about 50 nm. The crystallization mechanism of fcc-Al nanoparticles formation was evaluated. The results indicated the complex nature of the primary crystallization behavior of these amorphous alloys. Results of nanoindentation test revealed that controlled crystallization of the amorphous alloys significantly increased the strength, owing to the solute enrichment of the amorphous matrix.

© 2014 Elsevier B.V. All rights reserved.

1. Introduction

Amorphous alloys are a new class of advanced materials with a wide variety of applications and outstanding properties [1]. For structural applications, Al-based amorphous alloys are very attractive due to their high specific strength with good corrosion properties [2–5]. It is well established that in amorphous Al alloys (Al > 85 at%), fcc-Al nanocrystals are formed during crystallization of the amorphous matrix [6–8]. Various studies [9,10] have shown that precipitation of the aluminum nanocrystals significantly enhances the mechanical strength (> 150%) of the materials. The two-phase structure of crystalline particles embedded in an amorphous matrix provides a combination of properties that are very attractive for various engineering applications [11,12]. For this reason, many investigations have focused on studying the crystallization process of amorphous Al-based alloys [13–16].

Previous studies [17,18] have shown that the crystallization of fcc-Al nanoparticles in amorphous Al alloys is a complex process. By thermal analyses, it has been found that the activation energy of crystallization (E) is changed with continuation of the phase transformation, particularly at the late stage [17]. Microstructural studies also determined the effect of rare earth (RE) metals on the morphology of fcc-Al nanoparticles [19]. The presence of quench-in nucleus and glassy phase separation [20] on the mechanism of crystallization was reported as well. Moreover, hardness of amorphous Al-based ribbons was evaluated by the nanoindentation test and the effect of crystallization on the strength improvement was shown [21].

Although the effect of RE metals on the glass forming ability (GFA) and crystallization of amorphous Al alloys have been investigated frequently [22–24], from practical point of view, mixtures of RE metals (such as mischmetal, MM) are attractive because they are more accessible and economical compared to pure RE metals. Mischmetal is composed of several RE metals including Ce, La, Nd and Pr with a high negative heat of mixing with Al [25]. Therefore, the addition of MM can improve GFA of Al alloys in expense of more complexity of the crystallization process [26]. As similar to pure RE metals [19], the morphology of fcc-Al nanoparticles may also be

* Corresponding author at: Department of Materials Science and Engineering and Institute for Nanoscience and Nanotechnology, Sharif University of Technology, 14588 Tehran, Iran. Tel.: +98 21 6616 5261; fax: +98 21 6600 5717.

E-mail address: simchi@sharif.edu (A. Simchi).

changed depending on the concentration of MM. Therefore, more studies are required to evaluate the mechanisms and kinetics of crystallization in the amorphous Al alloys containing MM. Evaluations of the microstructural features and mechanical properties of these alloys are also very useful to employ controlled crystallization. The aim of this study is to investigate the effect of MM content on the thermal stability, mechanism of fcc-Al nanoparticles formation, and strength of amorphous Al–Ni–RE alloys. The activation energy of the crystallization process was determined by kinetic models and the effect of MM content on the morphology of precipitates was elaborated.

2. Materials and methods

Master alloys with a nominal composition of $\text{Al}_{90-x}\text{Ni}_{10}\text{MM}_x$ ($x=2, 4$) were prepared by arc melting of Al (99.99 wt%), Ni (99.99 wt%), and Ce MM (Ce:La:Nd:Pr=55:25:15:5) (RND Korea) under a high purity Ar atmosphere using Ti getter. Melting was performed several times to ensure compositional homogeneity of the alloying elements in the ingot. Amorphous ribbons with a width of 2–3 mm and a thickness of 25 μm were prepared by a single roll melt spinning machine. The tangential velocity of Cu wheel was 52 m/s. The phase characterization of the melt-spun ribbons was performed by X-ray diffraction (XRD) by utilizing monochromatic Cu $K\alpha$ radiation (New D8 advance, Bruker, Germany). High-resolution transmission electron microscopy (HRTEM),

JEOL 2100F, 200 kV, Tokyo, Japan) was used for the microstructural studies. TEM samples were fabricated by ion milling (PIPS 691, Gatan, USA) at 2 eV with a liquid nitrogen cooling stage. Differential scanning calorimetry (Perkin Elmer DSC-8, USA) in non-isothermal condition was utilized to study the crystallization process. Different heating rates (5–60 K/min) were utilized and the tests were performed under a high purity Ar gas flow using standard Al pan. Calibration of the instrument was carried out by pure indium and zinc (purity, 99.999 wt%). Two runs were performed consecutively for each experiment and the second run was used as the base line.

In some experiments, the ribbons were annealed inside the DSC instrument at different temperatures selected based on their thermal traces (after each exothermic peak). Annealing was performed at temperatures of 553 and 714 K for $\text{Al}_{88}\text{Ni}_{10}\text{MM}_2$ alloy and 553, 623 and 714 K for $\text{Al}_{86}\text{Ni}_{10}\text{MM}_4$ alloy with a heating rate of 20 K/min. In order to prevent excess crystallization and/or formation of new phases, the specimens were rapidly cooled (~ 150 K/min) from the annealing temperature without affording a dwelling time to examine microstructural changes by XRD and HRTEM. The reduced elastic modulus and nano-hardness of the amorphous and annealed ribbons were determined by a Tribolab nanoindentation system (Hysitron, Inc., Minneapolis, MN, USA) by using Berkovich diamond tip at the load control mode (5000 μN). Metallographic techniques were utilized to attain mirror smooth surfaces. Twenty-five indentations were carried out on each sample and the mean value of the measured data was considered as the nano-hardness of the materials.

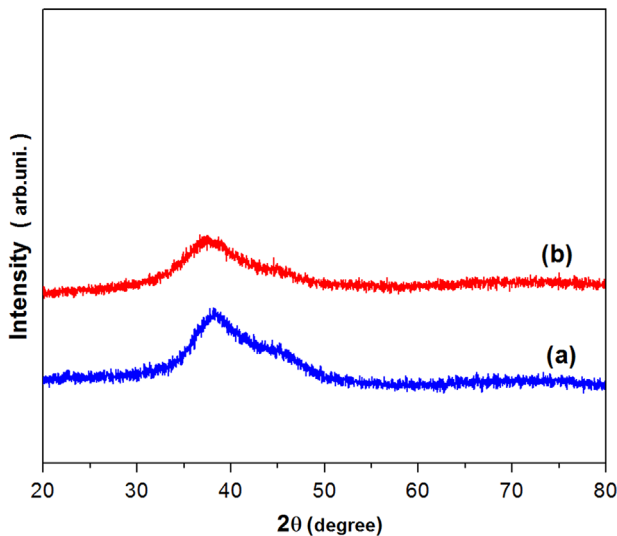


Fig. 1. XRD pattern of melt-spun (a) $\text{Al}_{88}\text{Ni}_{10}\text{MM}_2$ and (b) $\text{Al}_{86}\text{Ni}_{10}\text{MM}_4$ alloys.

3. Results

Fig. 1 shows XRD patterns of the melt-spun Al–Ni alloys containing 2 and 4 at% MM. The patterns exhibit a broad diffuse halo at $2\theta=30\text{--}50^\circ$ without any diffraction peak related to a crystalline phase. These patterns, which are typically observed in amorphous Al alloys, indicate that the ribbons are in an amorphous state. To further investigate the structure of the melt-spun ribbons, HRTEM was utilized. Bright-field TEM images and corresponding selected area diffraction (SAD) patterns of the ribbons are shown in Fig. 2. Featureless TEM images without contrast of crystalline phases and the diffused rings of SAD patterns confirm the amorphous state of the quenched alloys.

Fig. 3 shows DSC traces for the studied amorphous aluminum alloys at a heating rate of 20 K/min. The traces consist of a few exothermic steps, indicating different stages of the crystallization process. The DSC trace of $\text{Al}_{88}\text{Ni}_{10}\text{MM}_2$ alloy includes two exothermic peaks while the other shows three exothermic peaks (although second and third peaks are partly overlapped). The first exothermic event in $\text{Al}_{88}\text{Ni}_{10}\text{MM}_2$ alloy is tiny with an onset

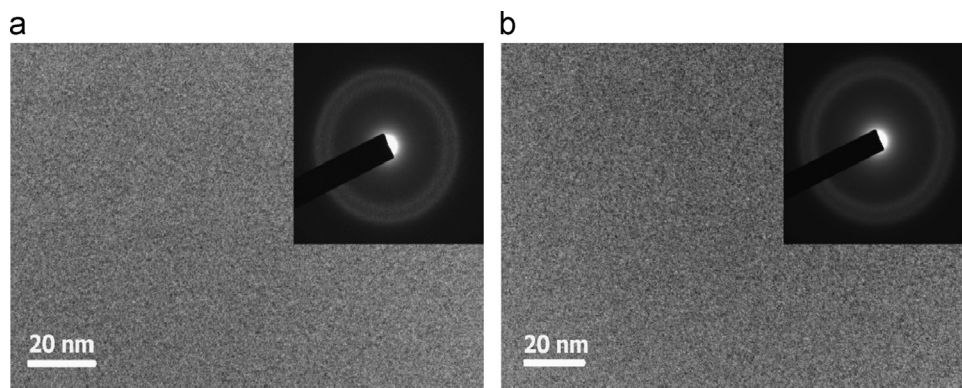


Fig. 2. Bright-field TEM images and corresponding SAD patterns of melt-spun (a) $\text{Al}_{88}\text{Ni}_{10}\text{MM}_2$ and (b) $\text{Al}_{86}\text{Ni}_{10}\text{MM}_4$ alloys.

temperature of ~ 404 K. At the higher MM concentration of 4 at%, the first exothermic peak is comparatively sharper and more intense with a shift in the onset temperature to ~ 504 K. It is important to mention that, no endothermic event related to a glass transition temperature could be detectable.

In order to identify the phases corresponding to each exothermic peak, the ribbons were annealed at different temperatures, as marked in Fig. 3 by arrows. XRD patterns of the ribbons after annealing are shown in Fig. 4. The results indicate that the first exothermic peak in both $\text{Al}_{88}\text{Ni}_{10}\text{MM}_2$ and $\text{Al}_{86}\text{Ni}_{10}\text{MM}_4$ alloys correspond to precipitation of fcc-Al nanoparticles (Fig. 4a). Bright-field TEM images of the annealed ribbons are shown in Fig. 5. In $\text{Al}_{88}\text{Ni}_{10}\text{MM}_2$ alloy, a high density of fcc-Al particles with an average size of ~ 12 nm is seen. In contrast, the microstructure of $\text{Al}_{86}\text{Ni}_{10}\text{MM}_4$ alloy consists of irregular Al crystals (~ 50 nm) embedded in the amorphous matrix. This observation indicates that the morphology and size of the crystallized phase are changed with increasing the MM concentration. At higher temperatures, the remaining amorphous matrix decomposes to $\text{Al}_{11}\text{MM}_3$ and Al_3Ni phases (Fig. 4b). It is pertinent to point out that the formation of Al-transition metal (TM) and Al-RE intermetallics is not practically interesting as these phases degrade the ductility of

the amorphous Al-TM-RE alloys [27]. Therefore, hereafter we will concentrate on the formation of nano-metric fcc-Al crystals through primary crystallization.

In order to explore the effect of MM concentration on the mechanical strength, nanoindentation test was afforded. Fig. 6 shows typical load-displacement curves for the amorphous and annealed ribbons. The mean values of the reduced elastic modulus and hardness of the alloys with consideration of their standard deviation (25 indents) are reported in Table 1. The mechanical strength of $\text{Al}_{86}\text{Ni}_{10}\text{MM}_4$ alloy is superior to that of $\text{Al}_{88}\text{Ni}_{10}\text{MM}_2$ alloy due to more concentration of MM. Partial crystallization of the alloys at 553 K enhanced the mechanical strength remarkably. Notably, the improvement was more pronounced for the alloy containing 4 at% MM. It is suggested that enrichment of the amorphous matrix by TM and RE metals due to the formation of fcc-Al particles is responsible for the strength enhancement [28]. The higher strength of $\text{Al}_{86}\text{Ni}_{10}\text{MM}_4$ alloy could thus be attributed to more solute enrichment of the matrix after crystallization, as similar to the amorphous Al alloys containing pristine RE metals [21].

4. Discussion

The presented results showed that the thermal stability of amorphous Al-Ni-MM alloys is improved by increasing the concentration of MM. As similar to the alloys containing pure RE elements [10], the strong interactions between the Al and RE atoms [25] are responsible for the higher thermal stability. In order to determine the role of MM on the thermal stability, the apparent activation energy of the crystallization process (E) was determined by the Kissinger method [29]:

$$\ln\left(\frac{\beta}{T_p^2}\right) = -\left(\frac{E}{RT_p}\right) + \text{constant} \quad (1)$$

where T_p is the peak temperature of crystallization, β the heating rate, and R the gas constant. Fig. 7 shows the DSC traces for the Al-Ni-MM alloys at various heating rates. The shifts in the peak temperatures with increasing the heating rate highlight the thermally-activated process of the crystallization [30]. From the slope of $\ln(\beta/T_p^2) - 1/T_p$ plots, one can calculate the value of the activation energy (Fig. 8). Values of activation energy for different stages of the crystallization process are reported in Table 2. The activation energy for the crystallization of fcc-Al nanoparticles in $\text{Al}_{88}\text{Ni}_{10}\text{MM}_2$ alloy is 140 ± 3 kJ/mol, which is close to the self-diffusion activation energy

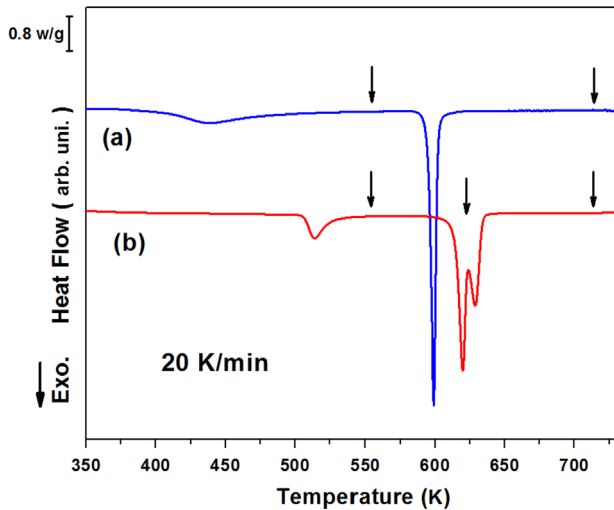


Fig. 3. Thermal analysis of (a) $\text{Al}_{88}\text{Ni}_{10}\text{MM}_2$ and (b) $\text{Al}_{86}\text{Ni}_{10}\text{MM}_4$ alloys at a heating rate of 20 K/min. The arrows indicate the selected annealing temperatures for studying the crystallization process.

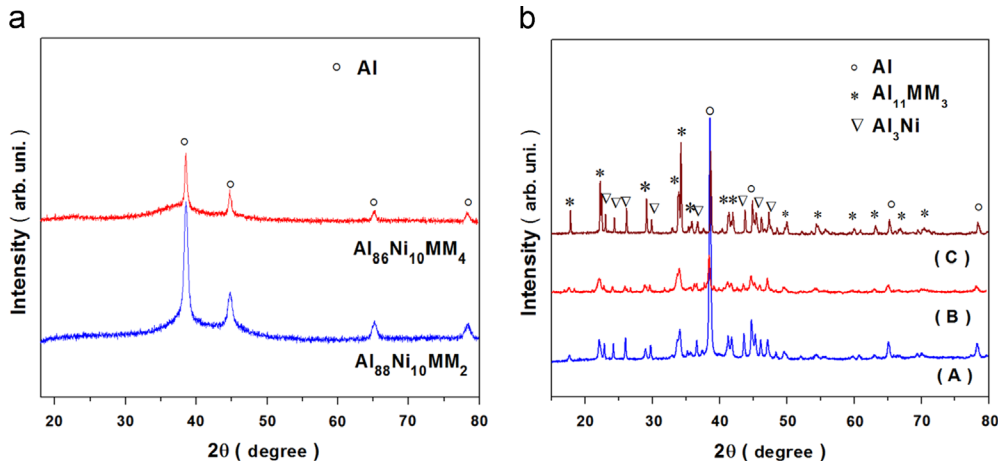


Fig. 4. XRD patterns of $\text{Al}_{90-x}\text{Ni}_{10}\text{MM}_x$ ($x=2, 4$) alloys after annealing at some selected temperatures. (a) Annealing at 553 K resulted in the formation of fcc-Al nanocrystals. (b) Annealing at higher temperatures forms Al-TM and Al-RE intermetallics. (A) XRD pattern of $\text{Al}_{88}\text{Ni}_{10}\text{MM}_2$ alloy after annealing at 714 K. (B) and (C) XRD patterns of $\text{Al}_{86}\text{Ni}_{10}\text{MM}_4$ alloy after annealing at 623 K and 714 K, respectively. The heating rate in these experiments was 20 K/min.

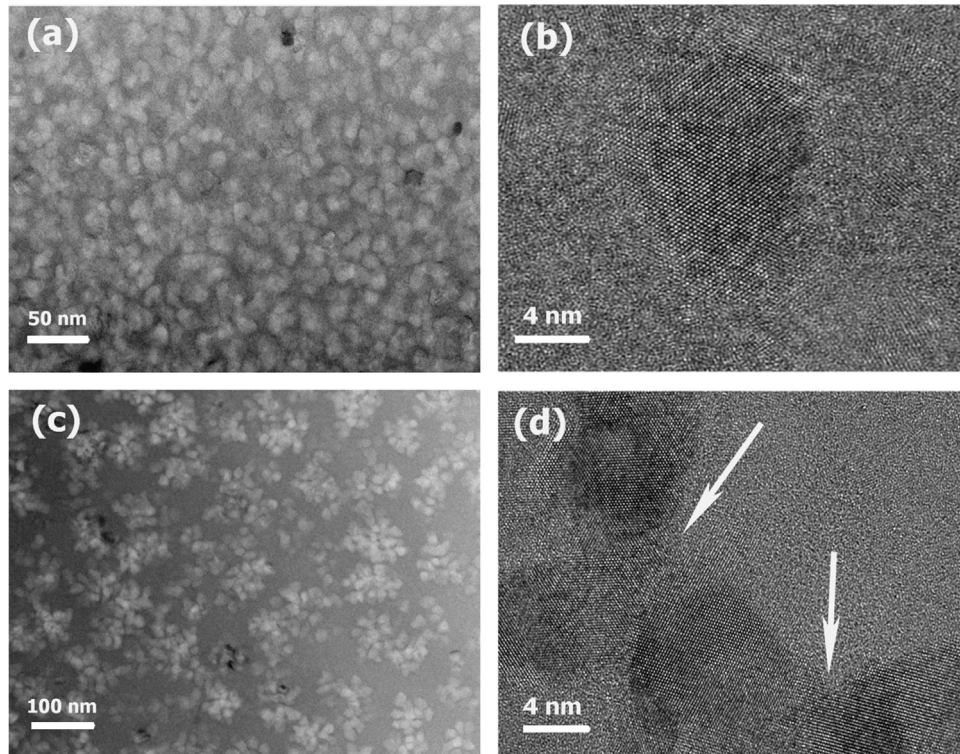


Fig. 5. Bright-field TEM images of annealed ribbons. (a) and (b) $\text{Al}_{88}\text{Ni}_{10}\text{MM}_2$ alloy annealed at 553 K. $\text{Al}_{86}\text{Ni}_{10}\text{MM}_4$ alloy annealed at (c) 553 K and (d) 518 K. The interface between crystallized fcc-Al particles are marked by arrows.

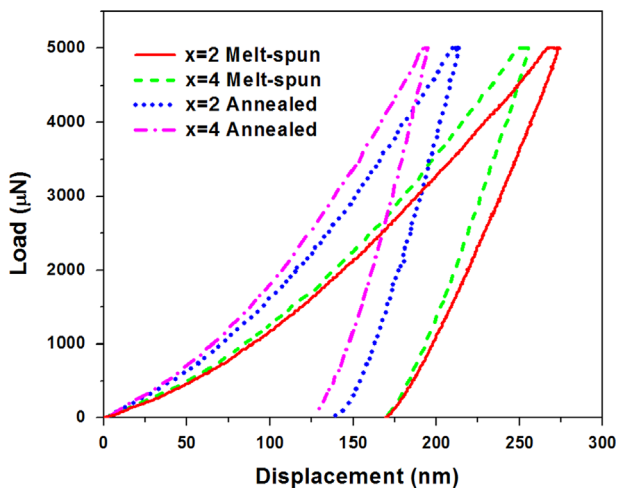


Fig. 6. Typical load–displacement curves of $\text{Al}_{90-x}\text{Ni}_{10}\text{MM}_x$ ($x=2, 4$) alloys under nano-indentation test. Annealing was performed at 553 K with a heating rate of 20 K/min.

Table 1

Results of nanoindentation test for the amorphous ribbons and annealed specimens at 553 K.

Alloy	Reduced elastic modulus (GPa)		Hardness (GPa)	
	Amorphous	Annealed	Amorphous	Annealed
$\text{Al}_{88}\text{Ni}_{10}\text{MM}_2$	46.0 ± 2.1	81.4 ± 1.4	3.52 ± 0.18	5.30 ± 0.14
$\text{Al}_{86}\text{Ni}_{10}\text{MM}_4$	59.9 ± 1.2	99.1 ± 1.3	3.82 ± 0.10	6.20 ± 0.17

of aluminum [31]. Increasing the MM content significantly enhanced the activation energy to 272 ± 5 kJ/mol that means higher thermally stability of the amorphous alloy. In other words, the more required

activation energy and higher onset temperature for the $\text{Al}_{86}\text{Ni}_{10}\text{MM}_4$ alloy could indicate an additional energetic cost for the formation of fcc-Al nanoparticles. It can be assumed that the activation energy of grain growth associated with the Al diffusion is not significantly different in both alloys (perhaps slightly higher in the $\text{Al}_{86}\text{Ni}_{10}\text{MM}_4$ alloy due to the higher concentration of the RE atoms) [32]. Therefore, it is suggestible that the primary crystallization of $\text{Al}_{88}\text{Ni}_{10}\text{MM}_2$ alloy (with activation energy close to that of the self-diffusion of Al) is performed without the nucleation barrier. This observation can be supported by the presence of medium range order (MRO) clusters in the amorphous alloy, as detected by fluctuation electron microscopy [33]. The presence of these clusters would operate as preferential sites for the nucleation of fcc-Al particles without long range diffusion of slow-diffusing solute atoms [34]. However, the higher stability of $\text{Al}_{86}\text{Ni}_{10}\text{MM}_4$ alloy reflects less concentration of MRO clusters; hence more energy is required for the nucleation and formation of the fcc-Al nanoparticles.

In order to determine the non-isothermal crystallization mechanism, the Blazquez et al. approach [35] was utilized:

$$\frac{d(\ln(-\ln(1-\alpha)))}{d(\ln((T-(T_p/2))/\beta))} = n \left(1 + \frac{E}{RT} \left(1 - \frac{T_p}{2T} \right) \right) \quad (2)$$

where α is the crystallized fraction at each specific temperature (T) and n the crystallization exponent. The variation of n as a function of α is shown in Fig. 9. The low n -values at the early stage indicate that the mechanism of crystallization is basically governed by the growth of the quench-in nuclei in the amorphous matrix [36]. The high number of MRO clusters also results in the formation of a high density of crystallized fcc-Al nanoparticles, as shown in Fig. 5a. Meanwhile, the small inter-particle spacing due to the high density of fcc-Al particles causes rapid overlapping of the enriched field; hence, soft impingement [32] retards further growth of the particles, forming round-shaped crystals (Fig. 5b). On the other hand, the higher values of n at the early stage for $\text{Al}_{86}\text{Ni}_{10}\text{MM}_4$ alloy indicate three-dimensional growth of the crystals with

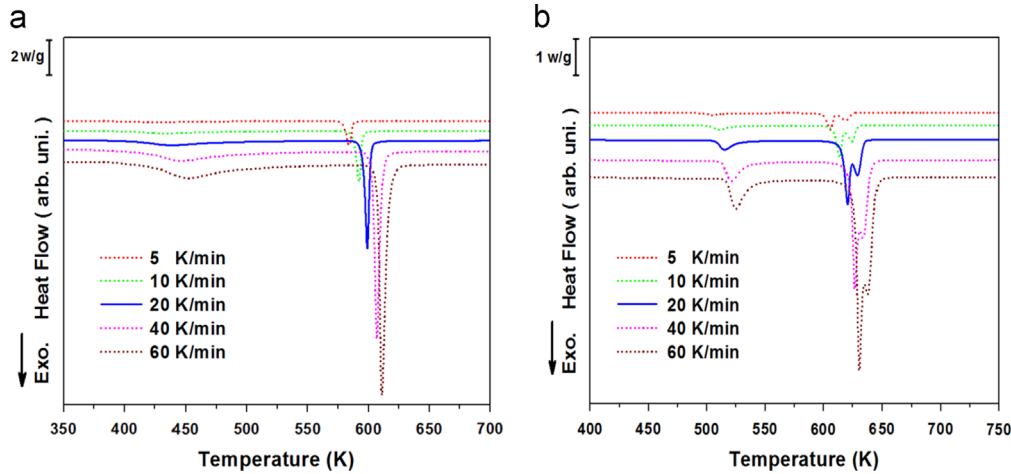


Fig. 7. DSC traces for (a) $\text{Al}_{88}\text{Ni}_{10}\text{MM}_2$ and (b) $\text{Al}_{86}\text{Ni}_{10}\text{MM}_4$ alloys at different heating rates.

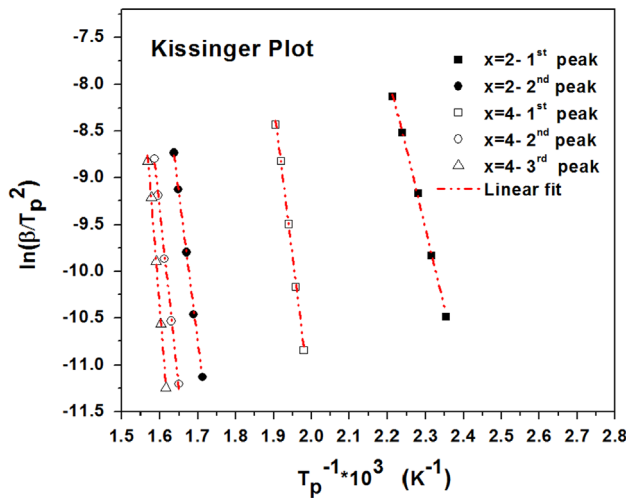


Fig. 8. Kissinger plots of crystallization sequences in $\text{Al}_{90-x}\text{Ni}_{10}\text{MM}_x$ ($x=2, 4$) alloys. The slope of straight lines is proportion to the activation energy of the primary (cubic symbols), secondary (circle symbols), and tertiary (triangle symbols) crystallization stages.

Table 2

Values of apparent activation energy (kJ/mol) for different crystallization stages in amorphous $\text{Al}_{88}\text{Ni}_{10}\text{MM}_2$ and $\text{Al}_{86}\text{Ni}_{10}\text{MM}_4$ alloys.

Material	First peak	Second peak	Third peak
$\text{Al}_{88}\text{Ni}_{10}\text{MM}_2$	140 ± 3	265 ± 5	–
$\text{Al}_{86}\text{Ni}_{10}\text{MM}_4$	272 ± 5	311 ± 10	424 ± 13

decreasing nucleation rate [36]. The lower density of Al nucleus in $\text{Al}_{86}\text{Ni}_{10}\text{MM}_4$ alloy compared to $\text{Al}_{88}\text{Ni}_{10}\text{MM}_2$ alloy implies higher chance of the particles to grow freely to form larger fcc-Al nanoparticles (Fig. 5c). Because of smaller nucleation barriers at the interfaces of existing crystals, heterogeneous nucleation of the fcc-Al nanoparticles, i.e. sympathetic nucleation, is susceptible [37]. As a result, irregular and cluster-like Al nanoparticles are formed (Fig. 5d).

5. Conclusions

Thermal stability, crystallization mechanisms, and mechanical properties of amorphous $\text{Al}_{90-x}\text{Ni}_{10}\text{MM}_x$ ($x=2, 4$) alloys were

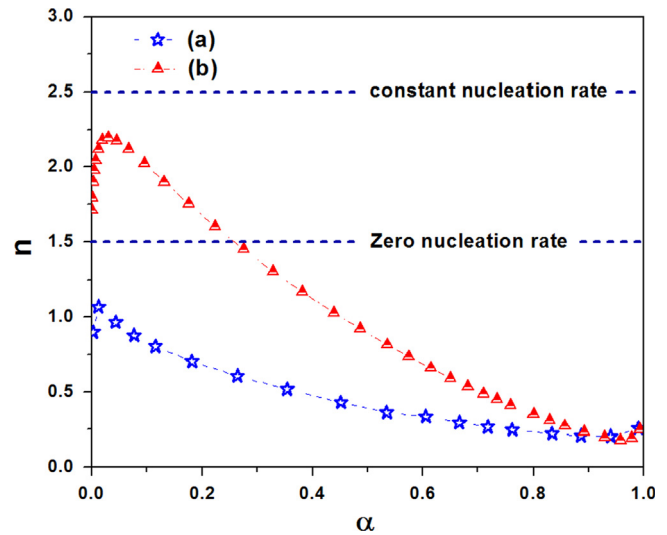


Fig. 9. Crystallization exponent (n) as a function of crystallized fraction (α) for amorphous (a) $\text{Al}_{88}\text{Ni}_{10}\text{MM}_2$ and (b) $\text{Al}_{86}\text{Ni}_{10}\text{MM}_4$ alloys.

investigated. The apparent activation energy of fcc-Al crystallization was found to be 140 ± 3 kJ/mol and 272 ± 5 kJ/mol for the alloys containing 2 at% and 4 at% MM, respectively. The activation energy of crystallization for $\text{Al}_{88}\text{Ni}_{10}\text{MM}_2$ alloy was determined to be close to that of aluminum self-diffusion, as an indicator of crystallization without a nucleation barrier (diffusion growth control mechanism). A high density of ultrafine fcc-Al particles (~ 12 nm) were formed after crystallization of the amorphous matrix at 553 K. The higher MM content in $\text{Al}_{86}\text{Ni}_{10}\text{MM}_4$ alloy enhanced its thermal stability, i.e. higher activation energy was required for crystallization. A morphology change from round-shaped Al particles to irregular cluster-like precipitates was observed with increasing the MM content. Coarser fcc-Al particles (~ 50 nm) were also formed. Nanoindentation test showed significant improvement in the strength of the amorphous alloys after crystallization. The effect of crystallization on the strength was more pronounced for the alloy containing more MM.

Acknowledgments

The authors acknowledge Dr. Sung Woo Sohn for his help in TEM studies and H.S. Oh for assistance in performing the

experiments. One of the authors (E.S. Park) was supported by the Center for Iron and Steel Research at RIAM and Engineering Research Institute at Seoul National University. RND Korea is appreciated for supplying the materials.

References

- [1] M.F. Ashby, A.L. Greer, *Scr. Mater.* 54 (2006) 321–326.
- [2] K. Song, X. Bian, X. Lv, J. Guo, G. Li, M. Xie, *Mater. Sci. Eng. A* 506 (2009) 87–93.
- [3] M. Wollgarten, K.L. Sahoo, J. Haug, J. Banhart, *Mater. Sci. Eng. A* 449–451 (2007) 1049–1051.
- [4] B.J. Yang, J.H. Yao, J. Zhang, H.W. Yang, J.Q. Wang, E. Ma, *Scr. Mater.* 61 (2009) 423–426.
- [5] C.H. Li, S.P. Pan, J.Y. Qin, Z.H. Zhang, W.M. Wang, *Corros. Sci.* 66 (2013) 360–368.
- [6] A.P. Tsai, T. Kamiyama, Y. Kawamura, A. Inoue, T. Masumoto, *Acta Mater.* 45 (1997) 1477–1487.
- [7] J.H. Perepezko, J. Hamann, R.J. Hebert, H. Rosner, G. Wilde, *Mater. Sci. Eng. A* 449–451 (2007) 84–89.
- [8] Y.E. Kalay, C. Yeager, L.S. Chumbley, M.J. Kramer, I.E. Anderson, *J. Non-Cryst. Solids* 316 (2003) 255–260.
- [9] H.S. Kim, *Mater. Sci. Eng. A* 304–306 (2001) 327–331.
- [10] A. Inoue, *Prog. Mater. Sci.* 43 (1998) 365–520.
- [11] Y.H. Kim, A. Inoue, T. Masumoto, *Mater. Trans. JIM* 31 (1990) 747–749.
- [12] T.T. Sasaki, K. Hono, J. Vireke, M. Wollgarten, J. Banhart, *Mater. Sci. Eng. A* 490 (2008) 343–350.
- [13] R.I. Wu, G. Wilde, J.H. Perepezko, *Mater. Sci. Eng. A* 301 (2001) 12–17.
- [14] Z.H. Huang, J.F. Li, Q.L. Rao, Y.H. Zhou, *Mater. Sci. Eng. A* 489 (2008) 380–388.
- [15] E. Illekova, P. Duhaj, P. Mrafko, P. Svec, *J. Alloy Compd.* 483 (2009) 20–23.
- [16] T.V. Kulikova, V.A. Bykov, A.A. Belozarova, A.M. Murzakaev, R.E. Ryltsev, *J. Non-Cryst. Solids* 378 (2013) 135–138.
- [17] F. Sun, T. Gloriant, *J. Alloy Compd.* 477 (2009) 133–138.
- [18] J.C. Foley, D.R. Allen, J.H. Perepezko, *Scr. Mater.* 35 (1996) 555.
- [19] N. Tian, M. Ohnuma, t. Ohkubo, K. Hono, *Mater. Trans. JIM* 46 (2005) 2880–2885.
- [20] D.H. Kim, W.T. Kim, E.S. Park, N. Mattern, J. Eckert, *Prog. Mater. Sci.* 58 (2013) 1103–1172.
- [21] M. Salehi, S.G. Shabestari, S.M.A. Boutorabi, *Mater. Sci. Eng. A* 586 (2013) 407–412.
- [22] H.W. Yang, P. Dong, J.Q. Wang, Y. Li, *Mater. Sci. Eng. A* 449–451 (2007) 273–276.
- [23] C.T. Rios, S. Surinach, M.D. Baro, C. Bolfarini, W.J. Botta, C.S. Kiminami, *J. Non-Cryst. Solids* 354 (2008) 4874–4877.
- [24] R. Sahu, A.J. Kailath, S. Chatterjee, K.L. Sahoo, *Mater. Sci. Eng. A* 527 (2010) 1339–1342.
- [25] A. Takeuchi, A. Inoue, *Mater. Trans. JIM* 46 (2005) 2817–2829.
- [26] D.V. Louzguine, A.R. Yavari, A. Inoue, *J. Non-Cryst. Solids* 316 (2003) 255–260.
- [27] M.A. Munoz-Morris, S. Suriñach, L.K. Varga, M.D. Baro, D.G. Morris, *Scr. Mater.* 47 (2002) 31–37.
- [28] T. Gloriant, D.H. Ping, K. Hono, A.L. Greer, M.D. Baro, *Mater. Sci. Eng. A* 304 (2001) 315–320.
- [29] H.E. Kissinger, *Anal. Chem.* 29 (1957) 1702–1706.
- [30] M.J. Starink, *Int. Mater. Rev.* 49 (2004) 191–226.
- [31] H.W. Jin, Y.J. Kim, C.G. Park, *J. Mater. Sci.* 36 (2001) 2089–2094.
- [32] D. Jacoviks, J. Rodriguez-Viejo, M.T. Clavaguera-Mora, *J. Phys. Condens. Matter* 17 (2005) 4897–4910.
- [33] W.G. Stratton, J. Hamann, J.H. Perepezko, P.M. Voyles, X. Mao, S.V. Khare, *Appl. Phys. Lett.* 86 (2005) 141910.
- [34] M.C. Gao, F. Guo, S.J. Poon, G.J. Shiflet, *Mater. Sci. Eng. A* 485 (2008) 532–543.
- [35] J.S. Blazquez, J.M. Barrego, C.F. Conde, A. Conde, S. Lozano-Perez, *J. Alloy Compd.* 544 (2012) 73–78.
- [36] J.W. Christian, *The Theory of Transformation in Metal and Alloys*, Pergamon press, Oxford, 1975.
- [37] H.I. Aaronson, G. Spanos, R.A. Masamura, R.G. Vardiman, D.W. Moon, E.S. K. Menon, M.G. Hall, *Mater. Sci. Eng. B* 32 (1995) 107–123.